Desalination and Water Treatment
www.deswater.com

doi: 10.5004/dwt.2017.21572

95 (2017) 342–354
November

Guar gum-coated iron oxide nanocomposite as an efficient adsorbent for Congo red dye

Jitendra Kumar Sahoo[a], Aniket Kumar[a], Juhi Rath[b], Tanuja Mohanty[c], Priyabrat Dash[a], Harekrushna Sahoo[a,*]

[a]*Department of Chemistry, National Institute of Technology Rourkela, Rourkela-769008, Sundergarh, Odisha, India, Tel. +91 6612462665; emails: sahooh@nitrkl.ac.in (H. Sahoo), kumarjitu8093@gmail.com (J.K. Sahoo), aniket.chemophilic@gmail.com (A. Kumar), dashp@nitrkl.ac.in (P. Dash)*
[b]*Institute of Minerals and Material Technology, Bhubaneswar, Khurda, Odisha, India, email: juhirath609@gmail.com*
[c]*School of Physical Science, Jawaharlal Nehru University, New Delhi 110067, India, email: tanujajnu@gmail.com*

Received 10 May 2017; Accepted 18 October 2017

ABSTRACT

Functionalized Guar gum (GG) on the surface of iron oxide (Fe_3O_4) nanoparticles was synthesized via conventional co-precipitation method. The nanocomposite was characterized by Fourier transform infrared, X-ray diffraction, field emission scanning electron microscopy, transmission electron microscopy, BET, vibrating sample magnetometer and zeta potential measurement. The efficiency of the nanocomposite was investigated towards the adsorption of different dyes such Congo red (CR), malachite green, methylene blue, methyl orange, Eriochrome Black T, methyl blue and Rhodamine B. Among which CR dye shows adsorption efficiency of 97% using the prepared nanocomposite. The presence of $–NH_2$ in the CR dye was responsible for the efficient adsorption, as it easily forms hydrogen bonding with the surface hydroxyl group of Fe_3O_4-GG. The optimum condition for dye removal efficiency using Fe_3O_4-GG was investigated by varying different factors such as the influence of pH, the initial concentration of dye, adsorbent dose and influence of contact time. Moreover, the adsorption procedure was studied with various adsorption isotherms (Langmuir, Freundlich, Temkin, Dubinin–Radushkevich and Elovich) and Langmuir isotherm was best fitted to the experimental data for CR removal with maximum adsorption capacity of 60.24 mg/g. The CR adsorption rate follows the pseudo-second order and within just 5 min maximum adsorption occurred. This material can be effectively used up to five consecutive runs. Hence, the synthesized Fe_3O_4-GG can be used as a good adsorbent for CR removal and reduce the pollution load in waste water.

Keywords: Guar gum; Magnetic iron oxide; Adsorption; Congo red dye

1. Introduction

Nowadays disposal of dyes and organic contaminants generated from the industries is the major source of water pollution that became a worldwide environmental concern. Industries such as paper, printing, cosmetics, plastics, leather, textile and petroleum release different types of dyes into the aquatic environment which causes water pollution [1,2]. These pollutant dyes and organic compounds are reported as toxic, carcinogenic and mutagenic in nature. Even with a few dyes discharged into the water system can affect the aquatic ecosystem and pose a serious problem to living organisms. Thus the removal of dye from the waste water is necessary and important before it is discharged into the environment [3]. Most of these dyes such as congo red (CR), malachite green (MG), methylene blue (MeB), methyl orange (MO), Eriochrome Black T (EBT), methyl blue (MB) and Rhodamine B (Rhb), etc. are frequently used in various industries.

* Corresponding author.

Among them CR dye, benzidine-based anionic bisazo dye, is most frequently used for various applications. This dye is responsible for several diseases such as human cancer, allergic dermatitis, skin irritation, and mutations [4]. Here, CR has been chosen as a model dye in view of its complex structure, restricted biodegradability, soundness towards the light and high dissolvability in water arrangement [5], so it is required to remove them during treatment. Till date, most of the techniques, such as photodegradation [6], adsorption [7], solvent extraction [8], coagulation [9], membrane filtration [10] and oxidizing agents [11], are used to take off poisonous chemicals from the dissolved aqueous solution. Among these, adsorption is a classical technique, because of its efficiency, economy and high level of effectiveness [12].

In past decades, various low-cost adsorbents such as palm kernel seed coat [13], magnetic alginate beads [14], chitosan [15], bagasse fly ash [16], clay mineral [17], biodegradable waste [18], agricultural waste [19] and industrial waste products [20] have been used as effective adsorbents for adsorption of carcinogenic dyes from different water bodies. A number of literature has also been reported towards the adsorption of Congo red on various adsorbent surfaces. Moreover, Kannan and Meenakshısundaram [21] have used activated carbon for the removal of congo red. Additionally, biogas waste has also been employed for the removal of Congo red from aqueous solution [22]. During the past decade, iron oxide has attracted much attention due to its wide range of applications such as biosensor development [23], biomedical engineering [24], drug delivery [25], bioseparation technologies [26] and other developments. Among various applications, iron oxides have been frequently used as adsorbent because of its several advantages such as low cost, extensive availability, good adsorption capacity and thermal stability [27,28]. Moreover, Fe_3O_4 has large specific surface area, reactive surface and easy magnetic separation after adsorption process. Therefore, the Fe_3O_4 nanoparticles can be a good selection for the adsorption of different dyes. The adsorption capacity of the Fe_3O_4 nanoparticle can be further improved by modifying it with various polysaccharides. There is some literature available where polysaccharides modified magnetic nanoparticles have been reported such as adsorption of reactive black due using chitosan modified graphite oxide [29], cobalt ferrite/activated carbon/alginate composite beads for adsorption of MB [30], removal of MeB dye using chitosan-g-poly (acrylic acid)/vermiculite hydrogel composites [31], etc.

Among all available polysaccharides, guar gum (GG) is the most important class of polysaccharide that can be a promising supporting material for adsorption due to its thermal stability and higher solubility. So we have explored the grafting of GG on to the surface of Fe_3O_4 nanoparticles to improve the hydrophilicity of Fe_3O_4 [32–35]. Therefore, the combined properties of both GG and Fe_3O_4 nanoparticle can be used for adsorption of toxic dyes. Till now GG modified Fe_3O_4 nanoparticle has not been studied thoroughly for the adsorption of various toxic dyes.

It is assumed that cross-linking of Fe_3O_4 nanoparticles with GG occurs via the 3,4-cis-hydroxy moiety, and thereby the formation of a three-dimensional network responsible for the gelation (the mechanism is illustrated in Fig. 1(a)). Besides having previous reports on the mechanistic points,

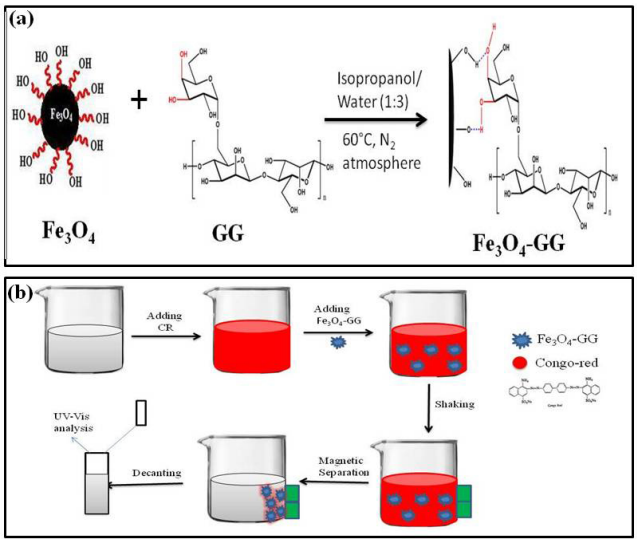

Fig. 1. (a) Schematic illustration of the synthetic procedure for Fe_3O_4-GG nanocomposite (b) Schematic illustration of the adsorption process for the CR using Fe_3O_4-GG.

which says that the active sites of GG are responsible for the cross-linking with Fe_3O_4, till date the mechanism is not clear [36]. The author observed entirely two different mechanisms: (a) a condensation reaction of OH groups on Fe_3O_4 nanoparticles and surface OH groups on GG and (b) an esterification reaction between Fe_3O_4 compounds and a hydroxyl group on GG. These two mechanisms do not impose any actual and clear mechanism. Therefore, it is still commonly believed that the formation of these nanoparticles only represents an undesired side reaction which actually reduces the activity of the cross-linker [37]. Thus, generally, the cross-linking mechanism is based on the ligand exchange reaction between Fe_3O_4 nanoparticles and GG [38].

Keeping this in mind our aim is to synthesize an efficient and active GG-coated Fe_3O_4 nanocomposite adsorbent and to study its activity towards the adsorption of various dyes. The enhanced adsorption efficiency is due to the presence of multiple numbers of hydrogen bonding selective binding site of Fe_3O_4-GG nanocomposite with the CR dye. The optimum experimental condition such as pH, contact time, adsorbent dose and initial dye concentration was demonstrated in order to give knowledge about adsorption kinetics, isotherm, thermodynamics and reusability of the prepared adsorbent (i.e., Fe_3O_4-GG). The present study showed that Fe_3O_4-GG nanocomposite could be a challenging adsorbent for dyes removal at large scale and at low cost.

2. Experimental setup

2.1. Materials

Citric acid monohydrate, MB, GG and EBT were purchased from Hi-Media (India). The anionic dyes such as MG, CR and Rhb were provided by Central Drug House Pvt. Ltd., New Delhi, India. Ferrous chloride anhydrous, isopropyl alcohol and aqueous ammonia solutions were purchased from Spectrochem, Mumbai, India. Ferric chloride anhydrous was procured from Finar reagent Company, Ahmedabad,

Gujarat, India. All other reagents were of analytical grade and used without further purification. All solutions were prepared with distilled water as per the requirement.

2.2. Synthesis of Fe_3O_4 nanoparticles

Fe_3O_4 nanoparticles were prepared by chemical co-precipitation method [39]. Briefly, 5 g of $FeCl_2$ and 11 g of $FeCl_3$ were dissolved in 100 mL deionized water and magnetically stirred vigorously for 2 h at 60°C under N_2 atmosphere. Then ammonia (NH_3. H_2O) solution (20 mL, 25% pure) was slowly added to the solution with an observation of the colour, which changes to black and the pH of final mixtures was controlled between the ranges of 10–11. The solution was heated to 70°C within 15 min then 4 g of citric acid monohydrate was added. After 1 h continuous stirring, it was removed and cooled at room temperature. The black precipitate was separated by a magnet and the nanoparticles were washed five times with deionized water then isopropyl alcohol and dried in an oven at 50°C overnight.

2.3. Synthesis of Fe_3O_4-GG nanocomposite

First we have taken 250 mg of GG powder and 50 mL of isopropyl alcohol in a round bottom flask then continuously stirred for 1 h under 60°C to facilitate the formation of a viscous gel. After the appearance of a completely homogeneous solution, then added 2.0 gm of Fe_3O_4 nanoparticles and stirred for 1 h at 60°C under N_2 atmosphere then 0.5 mL glutaraldehyde 25% was added into the mixture as a cross linker. After completion of the reaction, the pH 9–11 in the solution was adjusted to 1.0 mol/L NaOH. The mixture was stirred for 3 h and heated to 60°C then after followed by washing with distilled water (centrifuged at 6,000 rpm for 10 min) to remove any free particles. Finally, the obtained composite was dried at 80°C so as to obtain a dry powder of Fe_3O_4-GG nanocomposite, which was stored in desiccators.

2.4. Characterizations of Fe_3O_4-GG nanoparticles

Fourier transform infrared (FTIR) analysis of the nanocomposite was performed with KBr discs in the range 4,000–400 cm^{-1} on PerkinElmer (95277) FTIR Spectrometer Spectrum RX-I. Analytical study of the prepared composite was done using UV-Vis spectrophotometer (SHIMADZU-2450) and X-ray diffraction (XRD) measurements (Rigaku Dmax-2000 diffractometer using Cu Kα radiation source [λ = 0.15418 nm]). The morphology and nanostructure of the synthesized samples were obtained using field emission scanning electron microscopy (FE-SEM) by Nova NanoSEM/FEI. The morphology, composition and crystal structures of the samples were analyzed using transmission electron microscopy (TEM) on a JEOL 3010 instrument with a UHR pole piece using carbon coated 200 mesh copper grids at an acceleration voltage of 100–500 kV. The specific surface area, total pore volume and pore size distribution analysis were performed using 77 K on a Quantachrome Autosorb 3-B apparatus; respectively. The magnetic properties were measured on the MPMS 3 incorporates. All the samples were dispersed in deionized water and the zeta potential measurements were carried out with a zeta sizer nano (MALVERN ZS 90).

2.5. Batch adsorption experiment

CR dye uptake study was performed by using batch adsorption experiment on a magnetic stirrer (5MLH plus, REMI, Kolkata, India). An amount of 150 mg of the Fe_3O_4-GG nanocomposite with 100 mL of dye solution of the required concentration was taken in a 250 mL of conical flask and pH of the solution was adjusted by adding NaOH (0.1 M) or HCl (0.1 M) as required, then the mixture was stirred. The concentration of CR dye was analyzed by using UV-Vis (SHIMADZU-2450) spectrophotometer by monitoring the absorbance (495.7 nm). To get the optimum condition, the experiments were performed by varying adsorbent dose from 10 to 200 mg, initial dye concentration from 20 to 100 mg/L and pH from 2 to 12 and the solutions were taken out at a different time interval during the adsorption. From the above experimental data, we get the optimum conditions, that is, adsorbent dose of 150 mg, dye concentration of 60 mg/L at pH 6 shows the highest efficiency in 5 min. Later on, Fe_3O_4-GG nanoparticles were separated from the solution by exposing to magnet shown in Fig. 1(b).

The percentage of dye removal was calculated using Eq. (1):

$$\text{Percentage of removal} = \frac{C_0 - C_e}{C_0} \times 100 \quad (1)$$

And the equilibrium uptake was calculated using Eq. (2):

$$q_e = (C_0 - C_e) \times \frac{V}{W} \quad (2)$$

where C_0 is the initial concentration of the dye (mg/L), C_e is the final dye concentration (mg/L), q_e is the equilibrium adsorption capacity (mg/g), W and V represent the weight of adsorbent (g) and the volume of dye solution used (L), respectively. All the batch experiments were carried out in triplicate and results represented here are the average readings [40].

3. Results and discussion

3.1. FTIR analysis

FTIR spectra of Fe_3O_4, GG and Fe_3O_4-GG nanocomposite are presented in Fig. 2(A). In the case of Fe_3O_4, the peak at 569 cm^{-1} relates to Fe–O group [41,42], whereas GG exhibits the characteristic adsorption band at 3,383 cm^{-1} due to –OH stretching vibration of the polymer and water involved in hydrogen bonding [43]. The peak observed in the spectra at 800 and 1,200 cm^{-1} represents the highly coupled C–OH and C–O–C stretching mode of polymer back bone [44]. The peak 1,654 cm^{-1} attribute due to ring stretching of galactose and mannose. The weak bands around 770 cm^{-1} indicate the ring stretching and ring deformation of β-D-(1-4) and α-D-(1-6) linkages. The peak at 2,897 cm^{-1} and the marked bands at 1,059–1,033 cm^{-1} ascribed to C–H stretching and C–O stretching of GG, which indicated the formation of covalent bond between –OH groups of GG and Fe_3O_4. All these findings suggest that CR on Fe_3O_4-GG is held by chemical activation or chemisorptions [33,45].

3.2. XRD analysis

To determine the crystal structure and phase purity, the Fe_3O_4 and Fe_3O_4-GG nanocomposite were investigated by X-ray diffractometer shown in Fig. 2(B). The XRD patterns shows the characteristic peaks identified at 2θ = 30.09°, 35.42°, 43.05°, 56.94° and 62.51°, which are marked by their indices (220), (311), (400), (511) and (440), which agree well with the XRD pattern of JCPDS file no. 65-3107, respectively [46–48]. The diffraction peaks of Fe_3O_4 -GG are similar to the Fe_3O_4 nanoparticles, which reveal the crystal structure of high purity of Fe_3O_4 is well maintained after the coating of GG. The average crystallite size was calculated using the Debye–Scherrer formula:

$$D = \frac{0.94\lambda}{B\cos\theta} \tag{3}$$

where D is the average crystalline diameter, 0.94 is the Scherrer constant, λ is the X-ray wavelength, B is the angular line width of half-maximum intensity and θ is the Bragg's angle in degree. Here, the (311) peak of the highest intensity was picked out to evaluate the particle diameter of Fe_3O_4 and Fe_3O_4-GG. The D was calculated to be 4.2 and 6.8 nm, which is basically in accordance with the transmission electron micrographs discussed later.

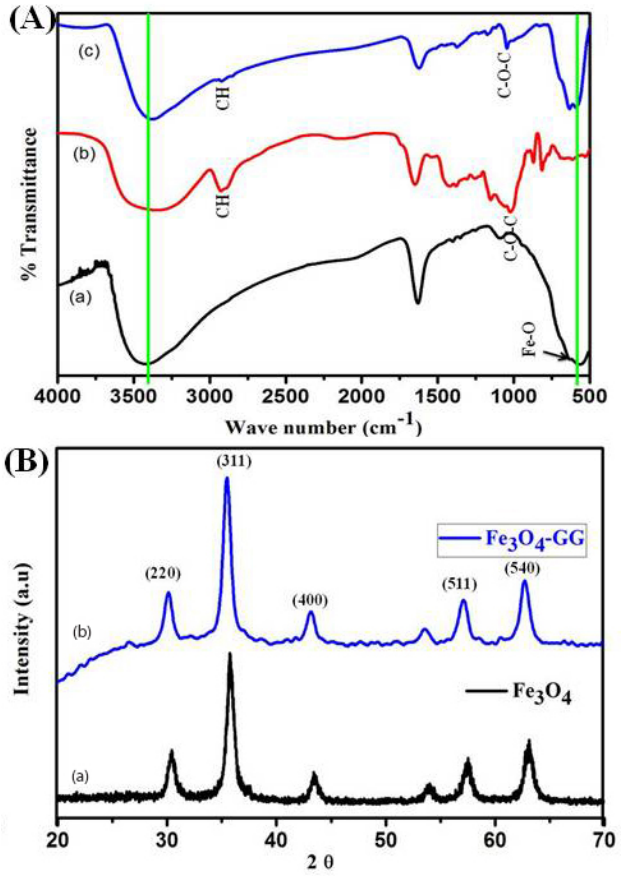

Fig. 2. (A) FTIR spectra of (a) Fe_3O_4 and (b) GG (c) Fe_3O_4-GG nanocomposite. (B) X-ray diffraction patterns of (a) Fe_3O_4 and (b) Fe_3O_4-GG nanocomposite.

3.3. FE-SEM analysis

The shape of the nanocomposite was investigated by FE-SEM and results are shown in Fig. 3. Figs. 3(a) and (b) show the FE-SEM micrograph of Fe_3O_4 and Fe_3O_4-GG nanocomposite, which has nearly uniform and spherical shape with homogenous dispersed nanoparticles. In both micrographs, size of the nanoparticles is almost same while some smaller and bigger size of the nanoparticles is also seen. To overcome this problem, later on, we are investigating TEM analysis for determining the size of the nanoparticles. In FE-SEM analysis, the magnetic nanoparticles were characterized using energy dispersive X-ray (EDX) analysis in order to identify the elemental components of the sample. Fig. 3(c) shows the EDX spectrum of Fe_3O_4-GG, which shows that various compositions were recorded. The effect illustrates strong peaks for Fe, C and O. The quantitative analysis indicated the molar presence of carbon (72.81%), oxygen (9.09%) and iron (18.08%) in the nanocomposite. Figs. 3(d)–(f) show energy dispersive study (EDS) of Fe_3O_4-GG nanocomposite which indicates the distribution of different element in different colour. That confirms well distribution of the element present in the nanocomposite.

3.4. TEM analysis

From the TEM analysis, we confirm the particles size and morphology of nanocomposite. Fig. 4 shows the TEM analysis of Fe_3O_4 nanoparticles and Fig. 6. shows GG-coated Fe_3O_4 nanocomposite. As we can see from the obtained micrograph, the prepared Fe_3O_4 nanoparticles and Fe_3O_4-GG nanocomposite are spherical in nature and some particles agglomerate, which is due to their high density and high specific surface area. The average particle size of Fe_3O_4 is 3.4 nm as shown in Fig. 5 whereas, Fig. 7 shows the distribution analysis for Fe_3O_4-GG and found to be 6.1 nm. After coating GG on the surface of Fe_3O_4, the particle size increases, and aggregation of particles reduces. Figs. 4(b) and 6(b) show selected area electron diffraction study (SAED) of Fe_3O_4 and Fe_3O_4-GG nanocomposite. In both, the case predicts a well-determined set of rings with bright spots, which indicates that both the Fe_3O_4 and GG-coated Fe_3O_4 nanocomposites are nanocrystalline in nature [49]. Fig. 6(c) shows the EDS micrographs of Fe_3O_4-GG nanocomposite indicating the distribution of different elements such as carbon, oxygen and iron. Fig. 6(d) demonstrates the distribution of all the element together and Figs. 6(e)–(g) show the element maps of iron (Fe), carbon (C) and oxygen (O) individually. The elemental mapping confirms that all the elements are well arranged.

3.5. BET analysis

The nitrogen sorption technique was performed to investigate the textural properties of Fe_3O_4 nanoparticles and Fe_3O_4-GG nanocomposite. In this analysis, we found that the BET surface area, pore volume and pore size of the Fe_3O_4 nanoparticles are 220 m^2/g, 0.99 cm^3/g and 6.5 nm, and 158 m^2/g, 0.398 cm^3/g and 15.5 nm for Fe_3O_4-GG nanocomposite. Fig. 8(a) shows that the nanocomposite has type IV isotherm (according to IUPAC classification). As we can see from Table 1, the surface area decrease after coating GG on the

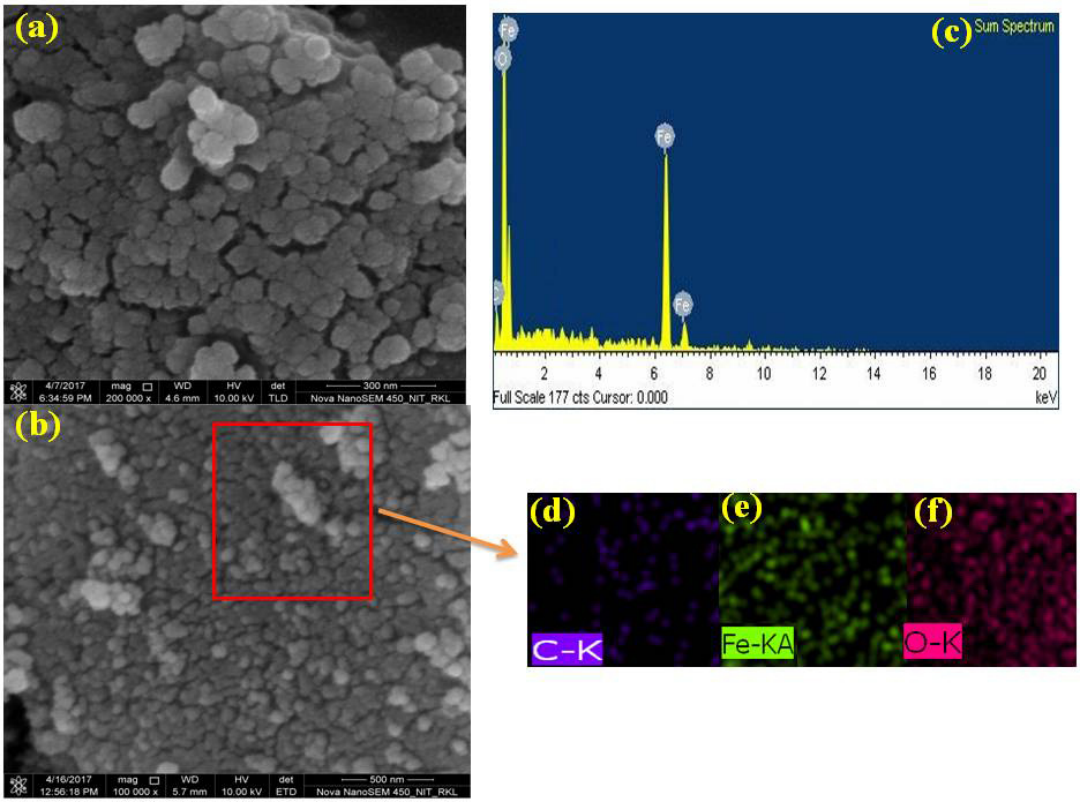

Fig. 3. Field emission scanning electron microscopy (FE-SEM) images of (a) Fe_3O_4, (b) Fe_3O_4-GG nanocomposite, (c) EDX spectra of Fe_3O_4-GG nanocomposite, (d–f) EDS data of Fe_3O_4-GG nanocomposite.

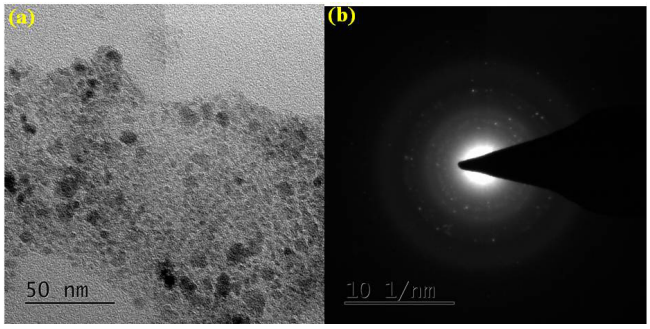

Fig. 4. (a) TEM of Fe_3O_4 nanoparticles (b) SAED pattern of Fe_3O_4 nanoparticles.

surface of Fe_3O_4 because the decrease in surface area can attribute the increase in crystal size of the nanoparticles by applying the Scherrer formula [50–53]. The result shows the immobilization of GG on the surface of Fe_3O_4 nanoparticles. The BET surface area and Barrett-Joyner-Halenda pore size distribution data confirm our prepared nanocomposite having mesoporous structure in nature and high surface area; these two properties having potential application in adsorption.

3.6. Magnetometer analysis

The magnetic property of Fe_3O_4 and Fe_3O_4-GG nanocomposite was analyzed by vibrating sample magnetometer.

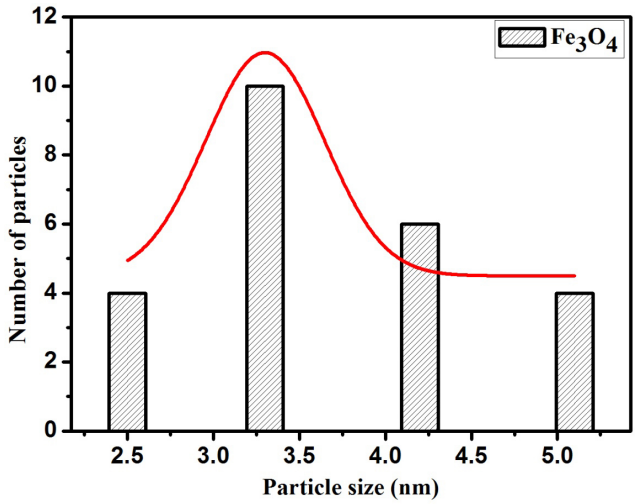

Fig. 5. Histogram of particle size distribution of Fe_3O_4.

Fig. 8(b) shows that the saturation magnetization curves of bare Fe_3O_4 nanoparticles and Fe_3O_4-GG can reach 51.95 and 22.73 emu/g at typical room temperature (298 K), (magnetic field ±5,000 G). As we can see from Fig. 8(b), these two samples show no remanence and coercivity. This indicates that the magnetic nanocomposites are paramagnetic in nature. However, the magnetic saturation value of the Fe_3O_4-GG nanocomposite became lower as compared with Fe_3O_4 nanoparticles, because of its higher molecular weight of

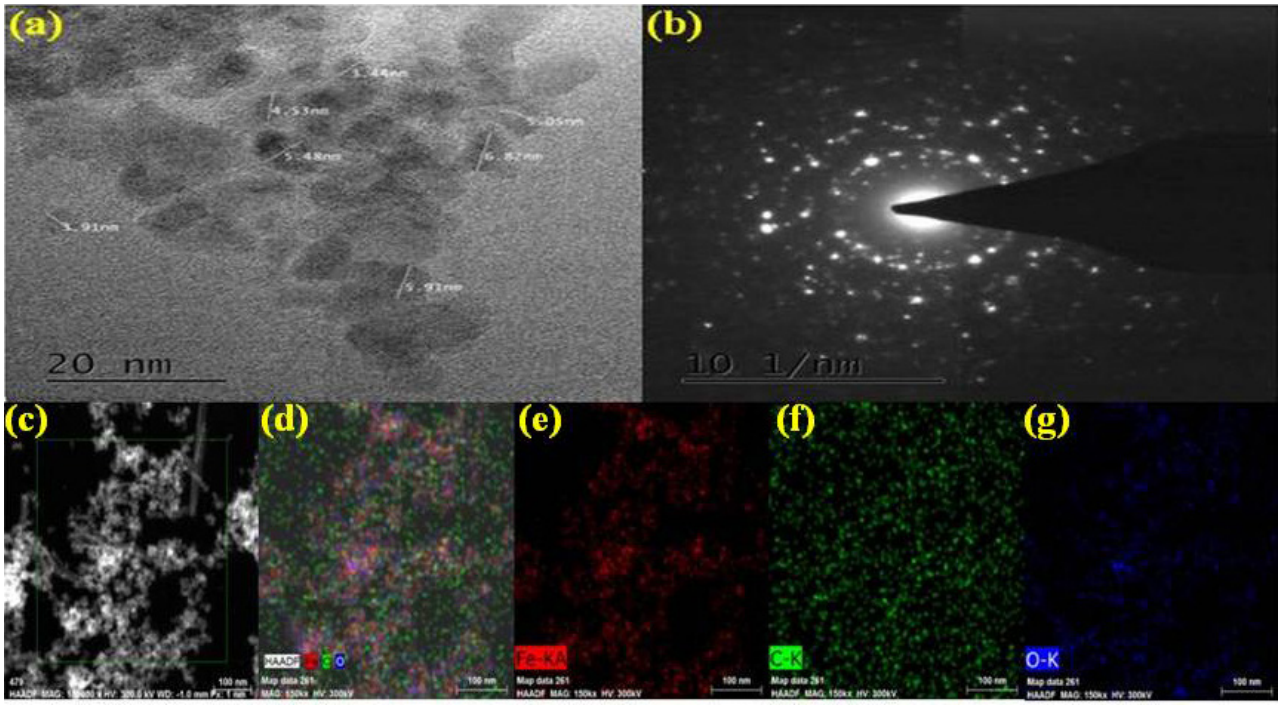

Fig. 6. (a) TEM image of Fe_3O_4-GG nanocomposites, (b) SAED pattern of Fe_3O_4-GG nanocomposites, (c) EDS mapping analysis of Fe_3O_4-GG nanocomposites.

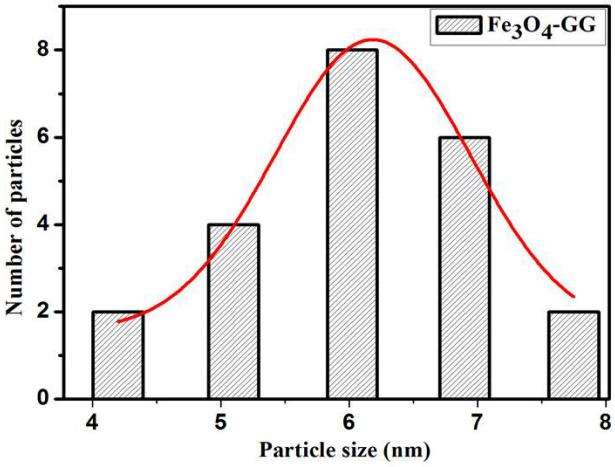

Fig. 7. Histogram of particle size distribution of Fe_3O_4-GG nanocomposite.

GG [31]. When an outside magnet was added, the Fe_3O_4-GG nanocomposite was attracted rapidly to the place close to the magnet in a few minutes and the solution almost purified (inset in Fig. 8(b)). The result suggested that Fe_3O_4-GG has good removal properties and could be easily separated from aqueous solution by using magnetic field [46].

3.7. Zeta potential analysis

Zeta potential measurement as a function of pH has been performed to confirm the surface charge properties. The zeta potential data of Fe_3O_4 and Fe_3O_4-GG at different pH are shown in Fig. 8(c). The Fe_3O_4 magnetic nanoparticles have positive charge at lower pH which decreases with increase in pH and became negative after its isoelectric point. The isoelectric point of the Fe_3O_4 and Fe_3O_4-GG nanocomposite is found to be 8.8 and 7.5, respectively.

4. Preferential adsorption of different dyes

The removal efficiency of various dyes (40 mg/L) by Fe_3O_4-GG nanocomposite (150 mg adsorbent dose) is shown in Fig. 8(d). The observation indicates the preferential adsorption of the dyes containing the amino group (–NH_2) group such as CR, which adsorbed with higher efficiency (~97% for CR) as compared with other available dyes such as MG (~43%), MeB (~11%), MO (~5%), EBT (~4%), MB (~5%) and Rhb (~4%) on the magnetic nanocomposite surface. Fe_3O_4-GG nanocomposite contain surface hydroxyl group that can be easily bonded to the dyes (i.e., CR and MG) containing –NH_2 group can form hydrogen electrostatic bonding with the surface hydroxyl group of the prepared Fe_3O_4-GG nanocomposite, which leads to improvement of the adsorption efficiency of discussed dyes as compared with other dyes, without –NH_2 group. The most dominating mechanism for adsorption of organic dyes on polymer-coated Fe_3O_4 nanocomposite surface is due to the surface complexation via electrostatic interaction under solution conditions [54,55].

5. Impact of different parameters on adsorption

5.1. Effect of dye concentration

Five various concentrations, that is, 20, 40, 60, 80 and 100 mg/L have been chosen to examine the effect of initial concentration of CR dye onto adsorbent, and the result

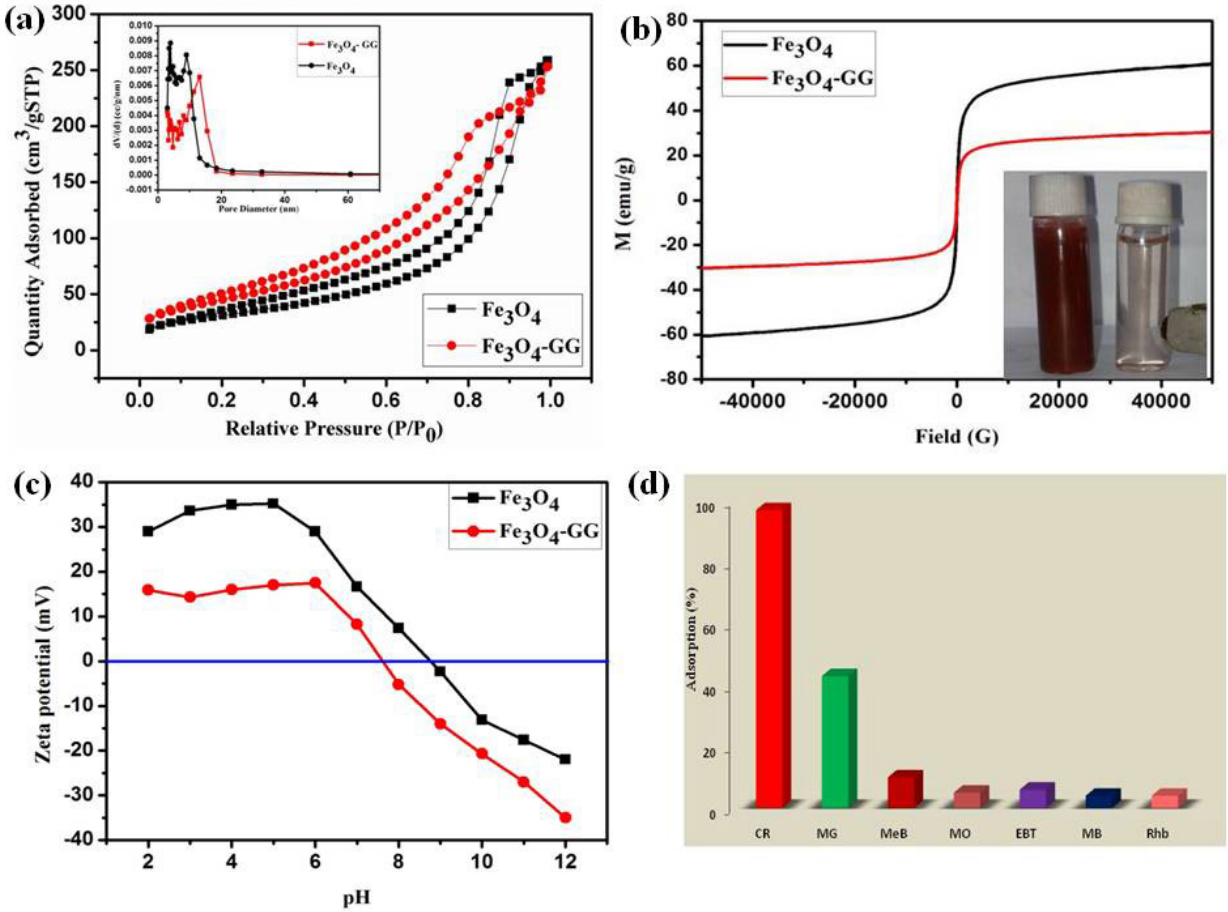

Fig. 8. (a) N_2 adsorption–desorption isotherm of Fe_3O_4 and Fe_3O_4-GG nanocomposite; (b) magnetization curve of Fe_3O_4 and Fe_3O_4-GG nanocomposite; (c) Zeta potential vs. pH of Fe_3O_4 and Fe_3O_4-GG nanocomposite; (d) preferential adsorption efficiency of different dyes on Fe_3O_4-GG nanoparticles.

Table 1
BET surface area, pore volume and pore size of Fe_3O_4 and Fe_3O_4-GG nanocomposite

Sample	BET surface area (m^2/g)	Pore volume (cm^3/g)	Pore size (nm)
Fe_3O_4	220	0.99	6.5
Fe_3O_4-GG	158	0.398	15.5

obtained at adsorbent dose 150 mg, pH 6 and 25°C (room temperature) are shown in Fig. 9(a). From this figure, it was observed that the percentage removal of CR at 20 and 40 mg/L dye concentration is approximately same but after increasing the concentration of the dye from 40 to 100 mg/L, the removal efficiency decreased from 97.45% to 51.49% because the numbers of active binding sites were saturated and the removal efficiency decreases [56]. The optimum dye concentration was an initiate to be 40 mg/L.

5.2. Effect of pH

pH assumes as an important parameter to control the removal efficiency of CR dyes by the Fe_3O_4-GG nanocomposite. From Fig. 9(b), it is observed that about 97.58% of CR (initial concentration of 40 mg/L) is removed at pH 6. The isoelectric point of the Fe_3O_4-GG nanocomposite is found to be 7.5. The Fe_3O_4-GG nanocomposite has positive surface charge at pH < 7.5 and electrostatic interaction occurred between the positively charged nanocomposite and negatively charged CR dyes. But at pH > 7.5, the surface charge becomes more negative due to the presence of excess OH^- ions on the adsorbent surface as shown in the following equation:

$$CH_2 - OH + OH^- \rightleftharpoons CH_2O^- + H_2O$$

Hence, there is a repulsive force existing in between the adsorbent surface and the negatively charged CR dye resulting in the reduction of the adsorption efficiency. Hence in acidic condition, an ionic complex is formed between the anionic dye (CR) molecules and the cationic polymer functionalized magnetic adsorbent surface.

5.3. Effect of adsorbent dose

The effect of Fe_3O_4-GG adsorbent dose on the removal of CR dyes from aqueous solution is illustrated in Fig. 9(c). The maximum CR dye removal efficiency for 40 mg/L solutions is

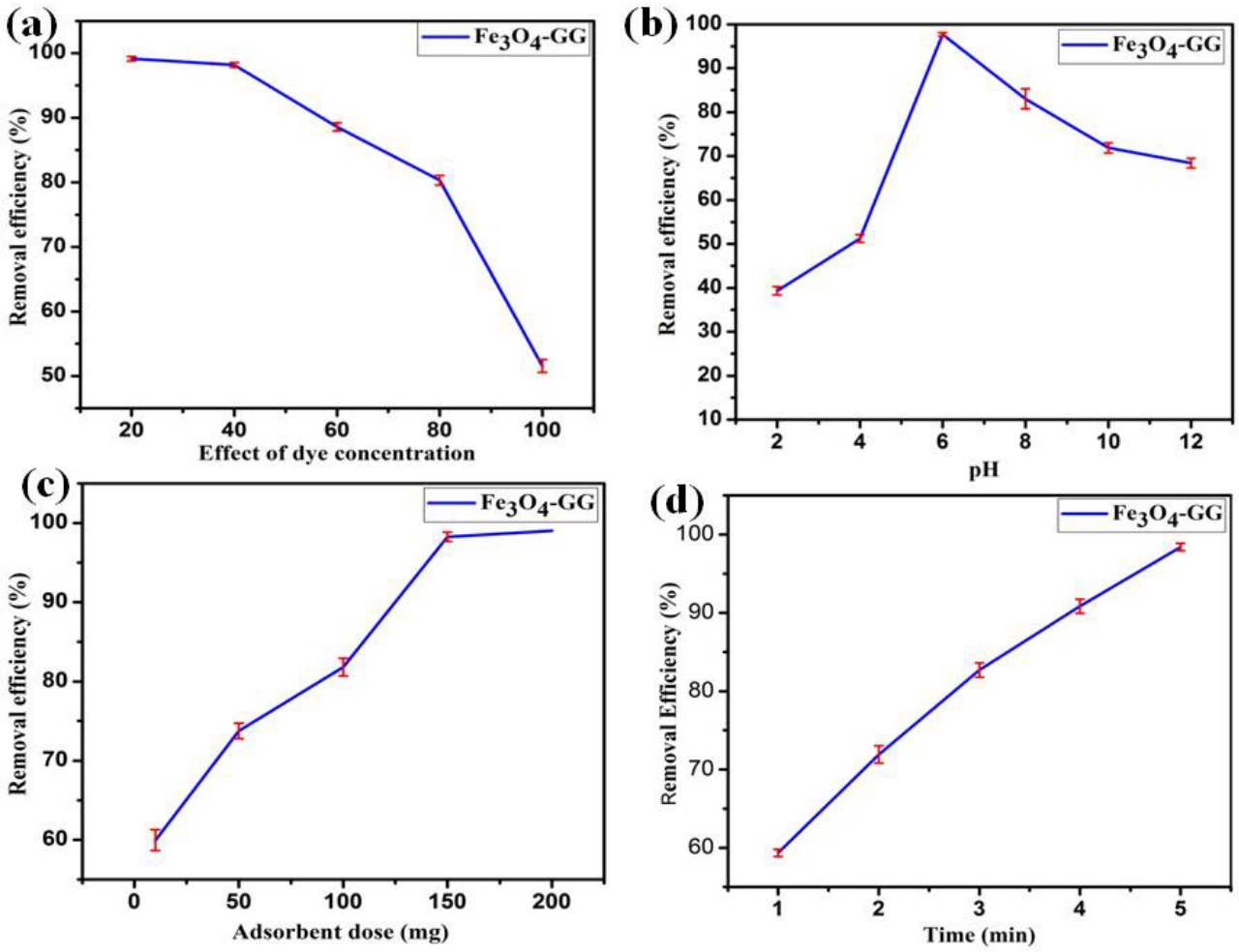

Fig. 9. (a) Removal of CR at different concentrations. (b) Effect of pH on the removal efficiency. The concentration of the adsorbent was 150 mg and the initial concentration of dye solution was 40 mg/L. (c) Effect of adsorbent dosage on adsorption of CR. (d) Effect of time on adsorption of CR.

61.3%, 74.2%, 81.6%, 97.4% and 97.5% with different adsorbent dose 10, 50, 100, 150 and 200 mg after 5 min, respectively. As shown in the graph the optimum adsorbent dose is 150 mg, after which it reached equilibrium. The obtained results confirm that on increasing the amount of adsorbent dose, dye adsorption efficiency was also increased due to the availability of more adsorbent surface area [35,40].

5.4. Effect of contact time

Contact time is one of the essential factors in the design of economical adsorption system. Fig. 9(d) reveals that dye uptake initial rate increased sharply with time and attained equilibrium (97.5%) within 5 min for CR dyes. This phenomenon shows that monolayer exposure of dye molecule at the external interface of the nanocomposite is formed during the adsorption process. The initial higher rate of removal is due to the larger surface area as well as the abundant active binding site of the nanocomposite [57,15]. After maximum removal, the adsorption rate was controlled by the rate of dye transport from external to internal pores of the nanocomposite materials.

6. Adsorption kinetics

In addition, kinetics studies would help to understand the mechanism of adsorption process and determine the rate limiting step. Two kinetic models (pseudo-first order and pseudo-second order) were introduced to simulate the experimental data. The details of pseudo-first-order model are presented below:

$$\log\left(q_e - q_t\right) = \log q_e - \frac{K_1}{2.303}t \tag{4}$$

where q_e is the adsorption capacity at equilibrium, q_t is the amount of dye adsorbed at time t. The parameter K_1 (min^{-1}) is the rate constant of pseudo-first-order adsorption. The plot of $\log(q_e - q_t)$ vs. t is illustrated in Fig. 10(a) (For CR) and the parameters such as K_1, q_e, and R^2 (correlation coefficient) values are listed in Table 2.

$$\frac{t}{q_t} = \frac{1}{K_2 q_e^2} + \frac{t}{q_e} \tag{5}$$

where the parameter K_2 (g/mg min) is the pseudo-second-order rate constant. The plot of t/q_t vs. t is illustrated in

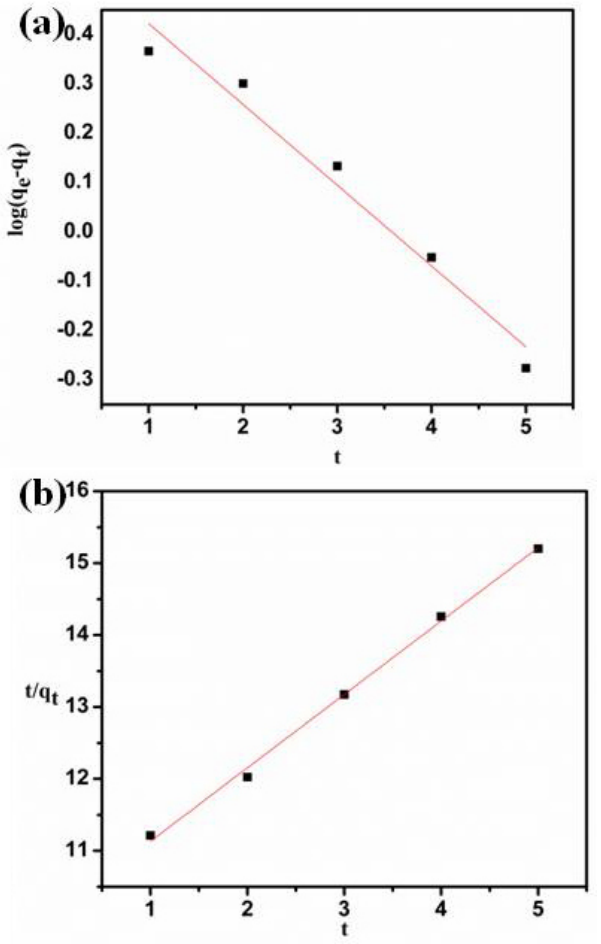

Fig. 10. Kinetic model parameters of CR adsorption on Fe_3O_4-GG (a) pseudo-first-order kinetic model and (b) pseudo-second-order kinetic model.

Table 2
Kinetics parameters for CR dye adsorption on Fe_3O_4-GG

Initial dye concentration (mg/L)	Pseudo-first-order kinetics			Pseudo-second-order kinetics		
	q_e (mg/L)	K_1	R^2	q_e (mg/L)	K_2	R^2
40 mg/L	3.85	0.07	0.95	5.26	2.71	0.99

Fig. 10(b) and the parameters such as K_2, q_e and R^2 (correlation coefficient) values are listed in Table 2. The kinetic models fit well with pseudo-second-order model due to higher R^2 value as compared with pseudo-first-order model. Our adsorption process follows pseudo-second-order model and is dependent on the amount of dye adsorbed on the surface of Fe_3O_4-GG nanocomposite at equilibrium. Generally, the pseudo-first-order is applicable to initial stage of adsorption that is why this model does not fit well with the whole range of contact time [40,58]. From the above the kinetic data, we confirm the adsorption process is due to chemisorptions which involved valence forces between dye anion and adsorbent.

7. Adsorption isotherm modelling

After adsorption kinetics, isotherm studies are investigated to describe the relationship between the dye molecules adsorbed at a given temperature per unit mass of the adsorbent (equilibrium adsorption capacity, q_e) and the liquid phase dye concentration (C_e). They provide very useful information about surface properties, adsorption mechanism and affinity of an adsorbent towards an adsorbate [59]. Different isotherm models have been used to describe the isotherm curve. Five adsorption isotherm models, Langmuir, Freundlich, Temkin, Dubinin–Radushkevich (D–R) and Elovich, were selected and the equation is listed below.

The linearized forms of the Langmuir equation are expressed as follows:

$$\frac{1}{q_e} = \frac{1}{bq_{\max}}\frac{1}{C_e} + \frac{1}{q_{\max}} \tag{6}$$

$$\frac{C_e}{q_e} = \frac{1}{q_{\max}}C_e + \frac{1}{bq_{\max}} \tag{7}$$

where C_e is the concentration of dye under equilibrium condition (mg/L), q_e is the amount of dye adsorbed (mg/g), the calculated value of b is the Langmuir constant (L/mg) and $q_{\max}$ is the maximum adsorption capacity (mg/g) are listed in Table 3. The Langmuir isotherm curve is plotted between $1/q_e$ and $1/C_e$ (Fig. 11(a)), hence Langmuir isotherm represents the homogeneous surface adsorption.

Freundlich isotherm suggests a heterogeneous surface or surface supporting sites of different energy of adsorption [59]. The non-linear form of Freundlich isotherm is expressed as:

$$\log q_e = \log K_f + \frac{1}{n}\log C_e \tag{8}$$

where n (heterogeneity factor) and K_f (mg/g) are the Freundlich constants indicating adsorption capacity and these parameters are calculated by plotting $\log q_e$ vs. $\log C_e$, Where $\log(K_f)$ is the intercept and $1/n$ is the slope of the line formed (Fig. 11(c)), respectively. The adsorption constant and correlation coefficient values are listed in Table 3. The n value larger than unity indicates that the adsorbate (dye) has been satisfactorily adsorbed on the adsorbent (Fe_3O_4-GG nanocomposite) and if $n < 1$, the adsorption is unfavorable.

Temkin and Pyzhev consider the effect of indirect adsorbent–adsorbate interaction on adsorption isotherm. The adsorption study is analyzed by a uniform distribution of the binding energies, up to some maximum binding energy [60,61]. The linear form of Temkin isotherm is expressed as:

$$q_e = B_1 \ln K_T + B_1 \ln C_e \tag{9}$$

$$B_1 = \frac{RT}{b} \tag{10}$$

where B_1 (KJ/mol) is the Temkin constant related to the heat of adsorption, K_T (L/g) is the isotherm constant, R is the gas constant (8.314 J/mol K) and T (K) is the absolute temperature. The parameters such as B_1, K_T and correlation coefficient

(R^2) are calculated by plotting the graph between q_e vs. lnC_e and are represented in Fig. 11(d), respectively.

The D–R is generally applied to resolve the nature of biosorption process as physical or chemical. The linear form of this isotherm [62] is:

$$\ln q_e = \ln q_m - K\varepsilon^2 \tag{11}$$

Table 3
Isotherm parameters for the adsorption of CR on to Fe_3O_4-GG at room temperature (300 K) and initial dye concentration 40 mg/L

Isotherm model	Parameters
Langmuir	q_m (mg/g) = 60.24
	b (L/mg) = 1.47
	R_L = 0.016
	R^2 = 0.99
Freundlich	K_f = 15.13
	n = 2.77
	R^2 = 0.96
Temkin	K_T (L/mg) = 20.58
	B_1 = 7.373
	R^2 = 0.92
Dubinin–Radushkevich	q_m (mg/g) = 46.08
	K (mol² K/J²) = –1.1674 × 10^{-4}
	E = 65.93
	R^2 = 0.97
Elovich	K_E = 6.63
	q_m = 12.19
	R^2 = 0.91

where K is a constant related to the adsorption mean free energy (mol²/KJ²), ε is the D–R isotherm constant and q_m is the maximum adsorption capacity (mg/g). The parameters such as K and q_m are calculated by plotting the graph between lnq_e and ε² is located in Fig. 11(e), respectively. The Polanyi potential (ε) can be determined by using Eq. (12):

$$\varepsilon = RT\ln\left(1+\frac{1}{C_e}\right) \tag{12}$$

where T (K) is the absolute temperature and R is the gas constant (8.314 J/mol K). The mean free energy of adsorption E is calculated by using the following formula:

$$E = \frac{1}{\sqrt{-2K}} \tag{13}$$

The highest adsorption capacity for CR is determined to be 46.08 mg/g. It can be seen that experimental q_m and calculated values are close to each other suggesting D–R partially over Langmuir isotherm. With the help of mean adsorption energy, information about the physical and chemical nature of the adsorption process is analyzed by the D–R isotherm model. Moreover, it is reported that when the value of E is <40 KJ/mol then the adsorption process is chemisorption mechanism [63]. When the value of E is below 8 KJ/mol or 8–16 KJ/mol the adsorption process indicates physiosorption [64]. Calculated E-value 65.93 KJ/mol suggests that the type of adsorption may be interpreted as chemical adsorption of CR onto Fe_3O_4-GG.

The equation defining the Elovich model is based on the kinetic principle assuming that the adsorption side increase

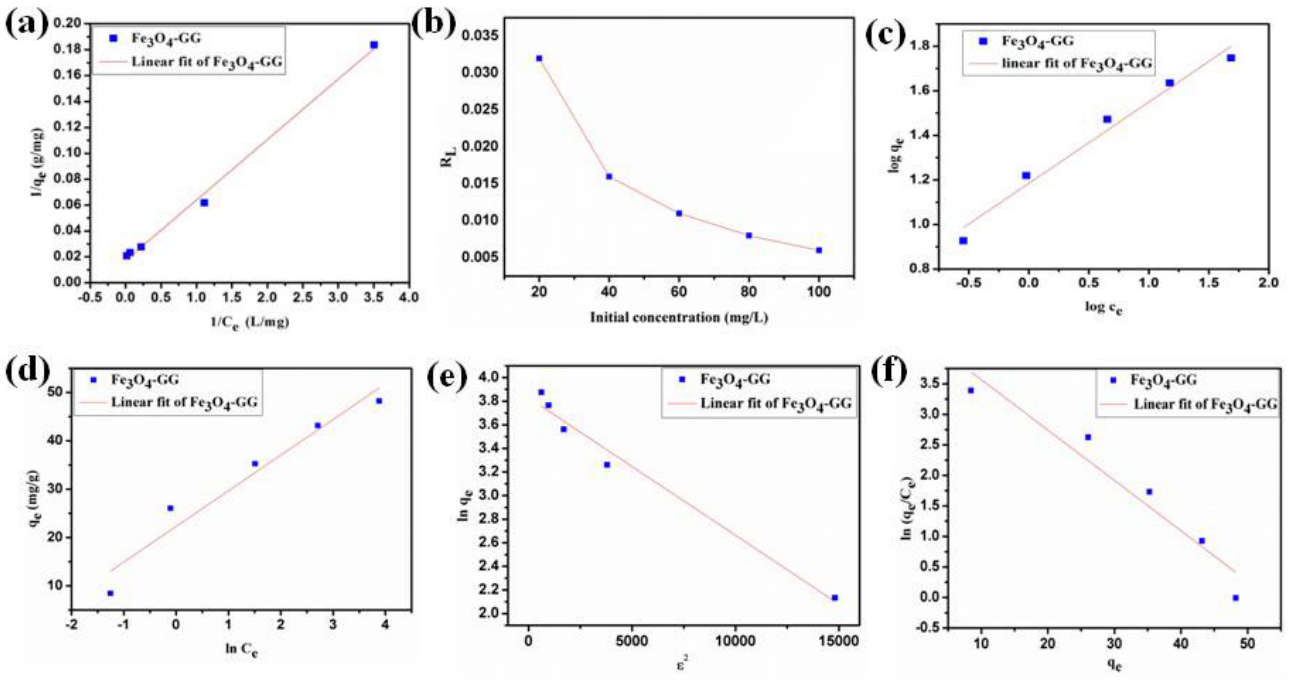

Fig. 11. (a) Langmuir isotherm plot, (b) effect of the initial concentration for CR adsorption on Fe_3O_4-GG, (c) Freundlich isotherm plot, (d) Temkin isotherm plot, (e) Dubinin–Radushkevich isotherm plot and (f) Elovich isotherm plot of CR on Fe_3O_4-GG.

exponential with adsorption, which implies a multi-layer adsorption. It is expressed by the relation:

$$\ln\frac{q_e}{C_e} = \ln K_E q_m - \frac{q_e}{q_m} \quad (14)$$

where q_m is the Elovich maximum adsorption capacity (mg/g) and K_E is the Elovich constant (L/mg) are calculated by plotting the graph between $\ln(q_e/C_e)$ and q_e are represented in Fig. 11(f).

All the isotherms are illustrated graphically in Fig. 11 and the isotherm parameters are listed in Table 3. From the obtained R_L value within the range 0 to 1, which confirms the adsorption process of CR on Fe_3O_4-GG was favorable at the condition being studied. However, the initial concentration increases from 20 to 100 mg/L as the R_L value decreases (Fig. 11(b)). From the Freundlich isotherm, the values of $1/n$ less than 1 represent a favorable adsorption [65]. The smaller value of the Temkin constant (B_1) suggested that adsorption of CR on Fe_3O_4-GG is favorable. The isotherm model with highest coefficient of correlation (R^2) value is regarded as the well fit of isotherm models. The comparison of coefficients indicates that the Langmuir isotherm fits more precisely (R^2 = 0.98) than the Freundlich isotherm (R^2 = 0.96), Temkin isotherm (R^2 = 0.92), Elovich isotherm (R^2 = 0.91) and D–R isotherm (R^2 = 0.97). The Langmuir adsorption isotherm model assumes monolayer formation between CR and Fe_3O_4-GG nanocomposite [66].

8. Comparative study of adsorption capacity with different adsorbents

The comparison study of highest adsorption limit of Fe_3O_4-GG nanocomposite with reported adsorbents has been examined to understand the effectiveness of the prepared nanocomposite as an adsorbent for the removal of anionic CR dye from aqueous solution. Table 4 reflects that q_{max} of synthesized Fe_3O_4-GG (60.24 mg/g for CR) is substantially higher than that of other reported adsorbents towards CR dye. This result indicates that Fe_3O_4-GG nanocomposite can be considered as a better adsorbent for the uptake of CR dyes from aqueous solution. As stated in Table 4, CR has higher adsorption rate with palm kernel seed coating material but the disadvantage of the material is that it cannot be regenerated for multiple applications. Whereas, overcoming the said disadvantage, our GG-based Fe_3O_4 nanocomposite can be regenerated for several cycles with an almost similar efficiency that can be shown in Fig. 8(d) [13–15,67].

9. Regeneration of dye-loaded adsorbent

The reusability of the nanocomposite (Fe_3O_4-GG) was studied with 40 ppm CR dye solution (pH = 6) mixed with 150 mg of Fe_3O_4-GG nanocomposite for 5 min. The dye-loaded sample was filtered and dried completely. Afterward, the adsorbent was washed with ethanol and several times with deionized water [68]. Five successive adsorption–desorption cycles were performed to find out the repeated use of the adsorbent as an efficient adsorbent as shown in Fig. 12.

10. Conclusions

A simple method has been developed for covalently coating GG on to the surface of Fe_3O_4 nanoparticles by using low-toxic and cost-effective precursors. The dye CR was adsorbed in much higher amounts as compared with MG, MeB, MO, EBT, MB and Rhb. The preferential adsorption phenomena could attribute to the presence of $–NH_2$ groups present in CR dye, which can bind easily with the surface hydroxyl groups of GG-coated magnetite nanoparticles. The optimum concentration of Fe_3O_4-GG nanocomposite is 150 mg/L, while the initial dye concentration 40 mg/L at pH = 6. Due to the paramagnetic behavior of the prepared nanocomposite, the magnetic adsorbent can be easily separated dye by using a small magnet. The result indicates that the removal of CR is over 97%. There are several advantages of the nanocomposite that play a crucial role for dye adsorption such as higher surface area, easy separation by exposing magnet, hydrodynamic volume and controlled growth of GG-coated Fe_3O_4 nanocomposite as well as multiple numbers of H-bonding sites of nanocomposite with dye molecules. The optimum concentration of Fe_3O_4-GG is 150 mg/L, while the initial concentration of CR is 40 mg/L at pH = 6. The result

Table 4
Comparison of adsorption efficiencies of Fe_3O_4-GG nanocomposite for removal of Congo red dye with different adsorbents

Dye	Adsorbent	q_{max} (mg/g)	References
Congo red	Magnetically modified fodder yeast cell	49.7	[14]
Congo red	Chitosan/ montmorillonite nanocomposite	54.52	[15]
Congo red	Chitosan-coated magnetic iron oxide	42.62	[67]
Congo red	Palm kernel seed coat	66.23	[13]
Congo red	Fe_3O_4-GG nanocomposite	60.24	Present study

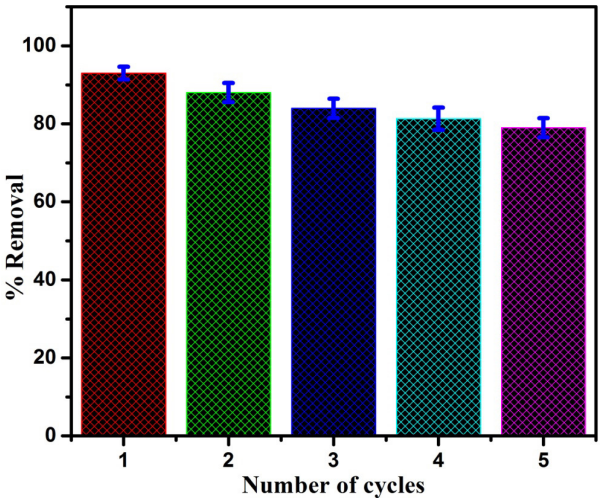

Fig. 12. Reusability of the adsorbent.

indicates that the removal of CR is over 97%. In addition, the adsorption capacity can be affected by ionic strength. The equilibrium data were found to fit better with the pseudo-second-order kinetics and Langmuir adsorption isotherm model. Finally, the recycling performance of adsorbent contributes a significant accomplishment toward sustainable improvement towards the dye-polluted water.

Acknowledgements

The authors are extremely grateful and sincerely acknowledge NIT Rourkela for providing the central instrumental facilities. The authors are also thankful to the Board of Research in Nuclear Sciences (BRNS), Government of India, for providing financial assistance.

References

[1] K. Golka, S. Kopps, Z.W. Myslak, Carcinogenicity of azo colorants: influence of solubility and bioavailability, Toxicol. Lett., 151 (2004) 203–210.
[2] N. Bao, Y. Li, Z.T. Wei, G.B. Yin, J.J. Niu, Adsorption of dyes on hierarchical mesoporous TiO_2 fibers and its enhanced photocatalytic properties, J. Phys. Chem. C, 115 (2011) 5708–5719.
[3] G.R. Chaudhary, P. Saharan, A. Kumar, S.K. Mehta, S. Mor, A. Umar, Adsorption studies of cationic, anionic and azo-dyes via monodispersed Fe_3O_4 nanoparticles, J. Nanosci. Nanotechnol., 13 (2013) 3240–3245.
[4] P. Frid, S.V. Anisimov, N. Popovic, Congo red and protein aggregation in neurodegenerative diseases, Brain Res. Rev., 53 (2007) 135–160.
[5] S. Chatterjee, M.W. Lee, S.H. Woo, Adsorption of Congo red by chitosan hydrogel beads impregnated with carbon nanotubes, Bioresour. Technol., 101 (2010) 1800–1806.
[6] A.N. Ejhieh, M. Khorsandi, Photodecolorization of Eriochrome Black T using NiSP zeolite as a heterogeneous catalyst, J. Hazard. Mater., 176 (2010) 629–637.
[7] M. Jiang, X. Jin, X. Lu, Z. Cheng, Adsorption of Pb (II), Cd (II), Ni (II) and Cu (II) onto natural kaolinite clay, Desalination, 252 (2010) 33–39.
[8] B. Galan, D. Castaneda, I. Ortiz, Integration of ion exchange and non-dispersive solvent extraction processes for the separation and concentration of Cr(VI) from ground waters, J. Hazard. Mater., 152 (2008) 795–804.
[9] J.C. Duan, Q. Lu, R.W. Chen, Y.Q. Duan, L.F. Wang, L. Gao, S.Y. Pan, Synthesis of a novel flocculant on the basis of crosslinked Konjac glucomannan-graft-polyacrylamide-co-sodium xanthate and its application in removal of Cu^{2+} ion, Carbohydr. Polym., 80 (2010) 436–441.
[10] A. Gürses, C. Doğar, M. Yalcin, M. Açikyildiz, R. Bayrak, S. Karaca, The adsorption kinetics of the cationic dye, methylene blue, onto clay, J. Hazard. Mater., 131 (2006) 217–228.
[11] H.-Y. Shu, C.R. Huang, M.C. Chang, Decolorization of mono-azo dyes in wastewater by advanced oxidation process: a case study of acid red 1 and acid yellow 23, Chemosphere, 29 (1994) 2597–2607.
[12] H.-Y. Zhu, Y.-Q. Fu, R. Jiang, J. Yao, L. Xiao, G.-M. Zeng, Novel magnetic chitosan/poly(vinyl alcohol) hydrogel beads: preparation, characterization and application for adsorption of dye from aqueous solution, Bioresour. Technol., 105 (2012) 24–30.
[13] N.A. Oladoja, A.K. Akinlabi, Congo red biosorption on palm kernel seed coat, Ind. Eng. Chem. Res., 48 (2009) 6188–6196.
[14] I. Safarika, L.F.T. Regoc, M. Borovskaa, E. Mosiniewicz-Szablewskae, F. Weydab, M. Safarikovaa, New magnetically responsive yeast-based biosorbent for the efficient removal of water-soluble dyes, Enzyme Microb. Technol., 40 (2007) 1551–1556.
[15] L. Wang, A. Wang, Adsorption characteristics of Congo Red onto the chitosan/montmorillonite nanocomposite, J. Hazard. Mater., 147 (2007) 979–985.
[16] V.K. Gupta, D. Mohan, S. Sharma, M. Sharma, Removal of basic dyes (rhodamine B and methylene 20 blue) from aqueous solutions using bagasse fly ash, Sep. Sci. Technol., 35 (2003) 2097–2113.
[17] B. Armagan, O. Ozdemir, M. Turan, M.S. Celik, Clay mineral process for colour removal of textile wastewater, J. Environ. Sci. Health Part A Toxic/Hazard. Subst. Environ. Eng., 38 (2003) 2251–2258.
[18] M.P. Elizalde-Gonzalez, A.A.P.-Cid, Removal of textile dyes from aqueous solution by adsorption on biodegradable wastes, Environ. Technol., 24 (2003) 821–829.
[19] K. Kadirvelu, M. Kavipriya, C. Karthika, M. Radhika, N. Vennilamani, S. Pattabhi, Utilization of various agricultural wastes for activated carbon preparation and application for the removal of dyes and metal ions from aqueous solution, Bioresour. Technol., 87 (2003) 129–132.
[20] B. Acemioglu, A. Samil, M.H. Alma, R. Gundogan, Copper(II) removal from aqueous solution by organosolv lignin and its recovery, J. Appl. Polym. Sci., 89 (2003) 1573–1541.
[21] N. Kannan, M. Meenakshısundaram, Adsorption of Congo Red on various activated carbons. A comparative study, Water Air Soil Pollut., 138 (2002) 289–305.
[22] C. Namasivayam, R.T. Yamuna, Removal of congo red from aqueous solutions by biogas waste slurry, J. Chem. Technol. Biotechnol., 53 (1992) 153–157.
[23] A. Fornara, P. Johansson, K. Petersson, S. Gustafsson, J. Qin, E. Olsson, D. Ilver, A. Krozer, M. Muhammed, C. Johansson, Tailored magnetic nanoparticles for direct and sensitive detection of biomolecules in biological samples, Nano Lett., 8 (2008) 3423–3428.
[24] E.H. Kim, H.S. Lee, B.K. Kwak, B.K. Kim, Synthesis of ferrofluid with magnetic nanoparticles by sonochemical method for MRI contrast agent, J. Magn. Magn. Mater., 289 (2005) 328–330.
[25] M.C. Urbina, S. Zinoveva, T. Miller, C.M. Sabliov, W.T. Monroe, C.S.S.R. Kumar, Investigation of magnetic nanoparticle-polymer composites for multiple-controlled drug delivery, J. Phys. Chem. C, 112 (2088) 11102–11108.
[26] S.J. Son, J. Reichel, B. He, M. Schuchman, S.B. Lee, Magnetic nanotubes for magnetic-field-assisted bioseparation, biointeraction, and drug delivery, J. Am. Chem. Soc., 127 (2005) 7316–7317.
[27] K. Wu, T. Liu, W. Xue, X. Wang, Arsenic(III) oxidation/adsorption behaviors on a new bimetal adsorbent of Mn-oxide-doped Al oxide, Chem. Eng. J., 192 (2012) 343–349.
[28] Y. Masue, R.H. Loeppert, T.A. Kramer, Arsenate and arsenite adsorption and desorption behavior on co-precipitated aluminum: iron hydroxides, Environ. Sci. Technol., 41 (2007) 837–842.
[29] N.A. Travlou, G.Z. Kyzas, N.K. Lazaridis, E.A. Deliyanni, Functionalization of graphite oxide with magnetic chitosan for the preparation of a nanocomposite dye adsorbent, Langmuir, 29 (2013) 1657–1668.
[30] L. Ai, M. Li, L. Li, Adsorption of methylene blue from aqueous solution with activated carbon/cobalt ferrite/alginate composite beads: kinetics, isotherms, and thermodynamics, J. Chem. Eng. Data, 56 (2011) 3475–3483.
[31] S. Liu, L. Zhang, J. Zhou, J. Xiang, J. Sun, J. Guan, Fiberlike Fe_2O_3 macroporous nanomaterials fabricated by calcinating regenerate cellulose composite fibers, Chem. Mater., 20 (2008) 3623–3628.
[32] R.Q. Long, R.T. Yang, Carbon nanotubes as superior sorbent for dioxin removal, J. Am. Chem. Soc., 123 (2001) 2058–2059.
[33] L. Yan, P.R. Chang, P.W. Zheng, X. Ma, Preparation and characterization of starch-grafted multiwall carbon nanotube composites, Carbohydr. Polym., 84 (2011) 1378–1383.
[34] J.L. Gonga, B. Wanga, G.M. Zenga, C.P. Yanga, C.G. Niua, Q.Y. Niua, W.J. Zhoua, Y. Liang, Removal of cationic dyes from aqueous solution using magnetic multi-wall carbon nanotube nanocomposite as adsorbent, J. Hazard. Mater., 164 (2009) 1517–1522.

[35] Y. Xie, D. Qian, D. Wu, X. Ma, Magnetic halloysite nanotubes/iron oxide composites for the adsorption of dyes, Chem. Eng. J., 168 (2011) 959–963.
[36] J. Kramer, R.K. Prud'homme, P. Wiltzius, P. Mirau, S. Knoll, Comparison of galactomannan crosslinking with organotitanates and borates, Colloid Polym. Sci., 266 (1988) 145–155.
[37] T. Hurnaus, J. Plank, Behavior of titania nanoparticles in cross-linking hydroxypropylguar used in hydraulic fracturing fluids for oil recovery, Energy Fuels, 29 (2015) 3601−3608.
[38] L.W. Teufel, J.A. Clark, Hydraulic fracture propagation in layered rock: experimental studies of fracture containment, Soc. Pet. Eng. J., 24 (1984) 19–32.
[39] A. Pourjavadi, A.A. Moghanaki, A. Tavakoli, Efficient removal of cationic dyes using a new magnetic nanocomposite based on starch-g-poly(vinylalcohol) and functionalized with sulfate groups, RSC Adv., 6 (2016) 38042–38051.
[40] H. Sun, L. Cao, L. Lu, Magnetite/reduced graphene oxide nanocomposites: one step solvothermal synthesis and use as a novel platform for removal of dye pollutants, Nano Res., 4 (2011) 550–562.
[41] S. Zhan, Y. Yang, Z. Shen, J. Shan, Y. Li, S. Yang, D. Zhu, Efficient removal of pathogenic bacteria and viruses by multifunctional amine-modified magnetic nanoparticles, J. Hazard. Mater., 274 (2014) 115–123.
[42] J.K. Sahoo, J. Rath, P. Dash, H. Sahoo, EDTA functionalized magnetic nanoparticle as a multifunctional adsorbent for Congo red dye from contaminated water, AIP Conf. Proc., 1832 (2017) 050087-1–050087-3.
[43] C. Fringant, I. Tvaroska, K. Mazeau, M. Rinaudo, J. Desbrieres, Hydration of alpha-maltose and amylose: molecular modelling and thermodynamics study, Carbohydr. Res., 278 (1995) 27–41.
[44] M. Kacurakova, A. Ebringerova, J. Hirsch, Z. Hromadkova, Infrared study of arabinoxylans, J. Sci. Food Agric., 66 (1994) 423–427.
[45] M.F. Abdullah, S.K. Ghosh, S. Basu, A. Mukherjee, Cationic guar gum orchestrated environmental synthesis for silver nano-bio composite films, Carbohydr. Polym., 134 (2015) 30–37.
[46] H. Shi, L. Tan, Q. Du, X. Chen, L. Li, T. Liu, C. Fu, H. Liua, X. Meng, Green synthesis of Fe_3O_4 nanoparticles with controlled morphologies using urease and their application in dye adsorption, Dalton Trans., 43 (2014) 12474–12479.
[47] K. Rajendran, S. Sen, Effect of capping agent on antimicrobial activity of nanoparticles, Der Pharmacia Lettre, 7 (2015) 37–42.
[48] B. Feng, R.Y. Hong, L.S. Wang, L. Guo, H.Z. Li, J. Ding, Y. Zhenge, D.G. Weif, Synthesis of Fe_3O_4/APTES/PEG diacid functionalized magnetic nanoparticles for MR imaging, Colloids Surf., A, 328 (2008) 52–59.
[49] A. Turpin, Y.V. Loiko, A. Peinado, A. Lizana, J. Campos, T.K. Kalkandjiev, J. Mompart, Polarization tailored novel vector beams based on conical refraction, Opt. Express, 23 (2015) 5704–5715.
[50] G.J. Copelloa, A.M. Mebert, M. Raineri, M.P. Pesenti, L.E. Diaz, Removal of dyes from water using chitosan hydrogel/SiO_2 and chitin hydrogel/SiO_2 hybrid materials obtained by the sol–gel method, J. Hazard. Mater., 186 (2011) 932–939.
[51] S. Ghorai, A. Sinhamahpatra, A. Sarkar, A.B. Panda, S. Pal, Novel biodegradable nanocomposite based on XG-g-PAM/SiO_2: application of an efficient adsorbent for Pb^{2+} ions from aqueous solution, Bioresour. Technol., 119 (2012) 181–190.
[52] Y.A. Shchipunov, T.Y. Karpenko, Hybrid polysaccharide-silica nanocomposites prepared by the sol-gel technique, Langmuir, 20 (2004) 3882–3887.
[53] Y. Liang, N. Guo, L. Li, R. Li, G. Ji, S. Gan, Preparation of porous 3D Ce-doped ZnO microflowers with enhanced photocatalytic performance, RSC Adv., 5 (2015) 59887–59894.
[54] L.C.S. Pirillo, M.L. Ferreira, E.H. Rueda, Removal of Fluorescein using different iron oxides as adsorbents: effect of pH, Spectrochim. Acta A, 71 (2008) 636–643.
[55] M.L.F.S. Pirillo, E.H. Rueda, Adsorption of Alizarin, Eriochrome Blue Black R, and Fluorescein using different iron oxides as adsorbents, Ind. Eng. Chem. Res., 46 (2007) 8255–8263.
[56] G. Crini, P.M. Badot, Application of chitosan, a natural aminopolysaccharide for dye removal from aqueous solution by adsorption process using batch studies, Prog. Polym. Sci., 33 (2008) 399–447.
[57] N. Sakkayawonga, P. Thiravetyana, W. Nakbanpoteb, Adsorption mechanism of synthetic reactive dye wastewater by chitosan, J. Colloid Interface Sci., 286 (2005) 36–42.
[58] G. Mckay, Y.S. Ho, The sorption of lead ions on peat, Water Res., 33 (1999) 578–584.
[59] S.J. Allen, G. Mckay, J.F. Porter, Adsorption isotherm models for basic dye adsorption by peat in single and binary component systems, J. Colloids Interface Sci., 280 (2004) 322–333.
[60] A.G. Sanchez, E.A. Ayuso, O.J.D. Blas, Sorption of heavy metals from industrial waste water by low-cost mineral silicates, Clay Miner., 34 (1999) 469–477.
[61] K.L. Wasewar, M. Atif, B. Prasad, I.M. Mishra, Adsorption of Zn using factory tea waste: kinetics, equilibrium and thermodynamics, Clean Soil Air Water, 36 (2008) 320–329.
[62] İ.H. Gubbuk, R. Gupb, H. Karaa, M. Ersoza, Adsorption of Cu(II) onto silica gel-immobilized Schiff base derivative, Desalination, 249 (2009) 1243–1248.
[63] X. Tang, Z. Li, Y. Chen, Adsorption behavior of Zn (II) on Chinese loess, J. Hazard. Mater., 161 (2009) 824–834.
[64] M.S. Onyango, Y. Kojima, O. Aoyi, E.C. Bernardo, H. Matsuda, Adsorption equilibrium modeling and solution chemistry dependence of fluoride removal from water by trivalent-cation-exchanged zeolite F-9, J. Colloid Interface Sci., 279 (2004) 341–350.
[65] A. Kausar, H. Nawaz, G. Mackinnon, Cost effective adsorption of aluminium and iron from synthetic and real wastewater by rice hull activated carbon, Am. J. Anal. Chem., 111 (2013) 124–133.
[66] M.K. Sahu, R.K. Patel, Removal of Safranin-O dye from aqueous solution using modified red mud: kinetics and equilibrium studies, RSC Adv., 5 (2015) 78491–78501.
[67] L. Zhou, C. Gao, W. Xu, Magnetic dendritic materials for highly efficient adsorption of dyes and drugs, ACS Appl. Mater. Interfaces, 2 (2010) 1483–1493.
[68] H. Zhu, M. Zhang, Y. Liu, L. Zhang, R. Han, Study of congo red adsorption on to chitosan coated magnetic iron oxide in batch mode, Desal. Wat. Treat., 37 (2012) 46–54.